Journal of Materials Chemistry C

ROYAL SOCIETY OF CHEMISTRY

PAPER

View Article Online
View Journal | View Issue

Check for updates

Cite this: J. Mater. Chem. C, 2025, 13, 18948

Flexible cold cathodes based on graphite nanoplatelet coatings on silicone rubber

Filippo Giubileo, *[a] Gianfranco Carotenuto,[b] Angela Longo,[b] Mariano Palomba,[b] Enver Faella,[c] Mariateresa Lettieri,[a] Loredana Viscardi,[ad] Kimberly Intonti,[ad] Arun Kumar,[e] Aniello Pelella,[f] Maurizio Passacantando[c] and Antonio Di Bartolomeo *[ad]

Received 11th June 2025,
Accepted 1st August 2025

DOI: 10.1039/d5tc02257f

rsc.li/materials-c

We report the fabrication and characterization of flexible cold cathodes based on graphite nanoplatelet (GNP) coatings on silicone rubber substrates. GNPs, synthesized *via* thermal exfoliation of graphite bisulfate and sonication in acetone, form nanostructured coatings with controlled roughness and thickness. Morphological, structural, and spectroscopic analyses confirm the presence of crystalline, few-layer graphitic domains. Field emission was locally probed by using a nanomanipulated tungsten tip anode inside a scanning electron microscope, revealing a turn-on voltage as low as 8.2 V and a field enhancement factor of ~80 at an anode–cathode distance of 100 nm. Emission characteristics are measured in different substrate curvature configurations: sharper bending alters the exposure of nanoplatelet edges, influencing the turn-on voltage and the field enhancement factor. The emitters exhibit excellent stability, robustness under strain, and thermally activated conduction behaviour with an activation energy of ~0.31 eV. Our findings demonstrate that GNP-coated silicone rubbers are a scalable, low-cost, and mechanically adaptive platform for next-generation vacuum microelectronics, enabling flexible, high-performance electron sources with nanoscale control and real-time tunability.

Open Access Article. Published on 04 August 2025. Downloaded on 12/21/2025 7:41:02 PM.
This article is licensed under a Creative Commons Attribution 3.0 Unported Licence.

1. Introduction

Field emission (FE), also referred to as cold emission,[1] is a quantum mechanical phenomenon in which electrons are emitted from the surface of a material (metal or semiconductor) under the influence of a strong electric field (of the order of 10^3 V μm^{-1}). Unlike thermionic emission, which requires significant heating to overcome the work function of the material, field electron emission takes place at room temperature. The effective potential barrier at the emitter/vacuum interface becomes lower and thinner due to the intense electric field, and electrons can tunnel into the vacuum through the barrier due to quantum effects. This makes field emission more energy-efficient with respect to thermionic emission; cold cathodes allow rapid activation, low power consumption, compact form factor, higher brightness, and narrower energy distribution of emitted electrons. Vacuum microelectronics and electron microscopy can benefit significantly from the lower energy requirements and improved control offered by field emission.[2] Furthermore, the ability to operate at ambient or near-ambient temperatures reduces the thermal degradation of components, extending their operational lifetime and enhancing reliability. Consequently, there is wide interest in using FE electron sources for several applications,[3,4] such as X-ray sources, field emission displays, electron microscopy, microwave amplifiers, UV generators, space thrusters, vacuum electronic devices, and electron beam lithography. In this context, we propose a flexible cold cathode architecture based on graphite nanoplatelet coatings on silicone rubber, enabling shape-dependent control of field emission properties.

The investigation of the FE phenomenon and the development of FE-based electron sources dates back to the derivation of the original model by Fowler–Nordheim.[5] Initially, metals were tested as field emitters, soon evidencing limitations related to their active nature and limited lifetime. With the advent of nanotechnology, it was soon evident that the increased aspect ratio of nanomaterials significantly enhances the electric field at the emitter surface, favouring the field emission process.[6] The field enhancement is particularly advantageous, as it reduces the

[a] CNR-SPIN Salerno, via Giovanni Paolo II, n. 132, 84084, Fisciano, Italy. E-mail: filippo.giubileo@spin.cnr.it
[b] CNR-IPCB, Institute for Polymers, Composites and Biomaterials, P.le E. Fermi, 1, 80055, Portici, Italy
[c] Department of Physical and Chemical Science, University of L'Aquila, Via Vetoio, Coppito, 67100, L'Aquila, Italy
[d] Department of Physics "E.R. Caianiello", University of Salerno, via Giovanni Paolo II n.132, 84084, Fisciano, Italy. E-mail: adibartolomeo@unisa.it
[e] Department SIMAU, Polytechnic University of Marche, Via Brecce Bianche 12, 60131, Ancona, Italy
[f] Department of Physics, University of Rome "Tor Vergata", Via Della Ricerca Scientifica, 1, 00133, Rome, Italy

This journal is © The Royal Society of Chemistry 2025

Open Access Article. Published on 04 August 2025. Downloaded on 12/21/2025 7:41:02 PM.
This article is licensed under a Creative Commons Attribution 3.0 Unported Licence.

required applied voltage/field to achieve emission, reducing the energy consumption of the process. Consequently, many nanostructures have been investigated in recent years, from 0D nanoparticles[7,8] to 1D nanotubes[9] nanowires,[10] and nanofibers[11] from 2D nanosheets[12] to 3D foams,[13] tetrapods[14] and nanoflowers.[15,16] Since the discovery of carbon nanotubes,[17] they have been considered promising as electron field emitters[18] because they can remain stable at extremely high emitted current densities due to tight covalent-bonds, as well as other carbon allotropes, including fullerenes, graphene and other graphitic nanostructures.[6,19] In particular, graphene nanoplatelets (GNPs) have emerged as a highly promising material for thermistors[20] and electron field emission applications,[21] combining thermal stability, mechanical robustness and high performance due to their unique structural properties, such as sharp edges, high aspect ratio, and multi-layered graphene composition. The interest in GNPs with respect to graphene comes from scalable production and lower costs while retaining impressive physical properties. In contrast to single-layer graphene, which requires complex and often costly fabrication and transfer processes, GNPs are easier to handle, can be deposited in large areas, and exhibit robust multilayer edge structures. These edges are key to enhancing field emission performance, as they support high local electric fields and ensure mechanical durability under operational stress. This nanoplatelet powder is typically obtained through liquid-phase exfoliation,[22] generally without additional centrifugation steps. Other common methods for GNP production include ball-milling, microwave exposure of acid-intercalated graphite, shear-exfoliation, and, more recently, wet-jet milling.[23–27] Structurally, GNPs are composed of single and few-layer graphene along with thicker graphite, positioning them between graphene and graphite. Commercial GNPs consist of a mix of single layers, few-layer structures, and nanostructured graphite, with thicknesses ranging from 0.34 to 100 nm within the same batch.

It has been reported that GNP field emitters fabricated by a screen-printing method showed a turn-on electric field of 1.77 V μm^{-1} and an emission current density of up to 39 mA cm^{-2}.[21] Their robustness was demonstrated by stable emission with only a 36% degradation over several hours under testing conditions, highlighting their potential for FE devices. Successively, a GNP-based paste field emitter built entirely from carbon-based components, including GNPs, graphite nanoparticles, and binders, has been developed on a graphite rod substrate.[28] The emitter showed good electron emission with a turn-on field of about 2.1 V μm^{-1}, a maximum current density of about 84 mA cm^{-2} at a 2000 μm cathode–anode separation distance and current stability with a degradation rate of around 10%. Despite the success of these devices, the development of GNP based flexible field electron emitters still remains a challenge.

Flexible cold cathodes are gaining increasing attention for their potential in next-generation electronics, where adaptability and durability are crucial.[29] Silicone rubber has proven to be an ideal flexible substrate for such applications, providing both mechanical flexibility and chemical compatibility with nanomaterials like graphene.[30] Consequently, the integration of GNPs onto silicone substrates represents a promising solution towards the development of innovative flexible cathodes.

In this work, we demonstrate flexible cold cathodes based on graphite nanoplatelet coatings on silicone rubber substrates, offering a scalable route to high-performance, mechanically adaptive electron sources. We report comprehensive morphological and electrical characterization of the coating. Field emission is locally investigated with nanoscale precision using a tip-shaped anode under high vacuum conditions, enabling quantitative analysis of the emission parameters as a function of anode–cathode distance and substrate curvature. The impact of mechanical deformation on the emission behaviour is explored, highlighting the changes in emission properties due to curvature-induced edge exposure. These results establish GNP-coated elastomers as a promising platform for next-generation flexible vacuum electronic devices.

2. Experimental section

Graphite nanoplatelets were prepared by using commercial graphite bisulphate (Asbury, NJ, USA). A schematic of the preparation process is shown in Fig. 1. The expandable graphite bisulphate was first thermally treated in a muffle furnace (thermal shock at 750 °C, 3 min) and the achieved expanded graphite filaments were dispersed in acetone under stirring and then shortly treated by sono-acoustic energy in an ultrasonic bath at room temperature (20 KHz, 200 W). The obtained colloidal suspension was allowed to completely dry overnight, thus leading to a spongy solid, that was successively mechanically powdered.[31,32] To prepare a quickly drying GNP paste, the achieved GNP powder was mixed with ethanol (the paste composition was *ca.* 33 g l^{-1}). This GNP-based

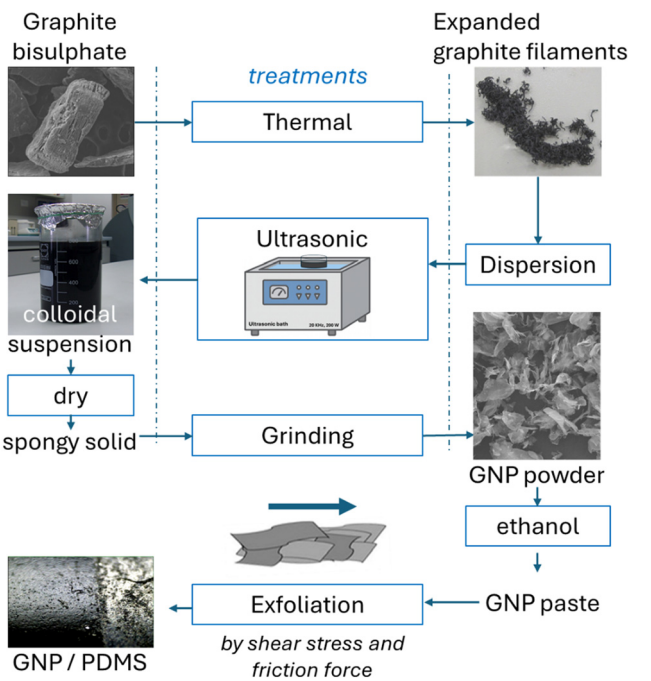

Fig. 1 Schematic representation of the preparation process of the graphite nanoplatelets (GNPs).

Open Access Article. Published on 04 August 2025. Downloaded on 12/21/2025 7:41:02 PM.
This article is licensed under a Creative Commons Attribution 3.0 Unported Licence.

paste was rubbed between the surfaces of two foils of a commercial silicon rubber (PDMS), until ethanol was completely evaporated. For the morphological/structural characterization and the electrical measurements rectangular specimens (5 mm × 10 mm) were fabricated by cutting the prepared GNP-coated silicon rubber foil.

3. Results and discussion

3.1 GNP characterization

The morphological and structural characterization of the GNP coating was performed using a Zeiss scanning electron microscope (SEM), a Veeco Dektat stilus profilometer, and a Nanosurf atomic force microscope (AFM).

SEM analysis revealed a layered surface morphology with distinguishable graphene nanoplatelet sheets distributed across the silicone rubber substrate (Fig. 2a). The imaging confirmed the presence of overlapping platelet structures, which is indicative of the effective deposition of the GNP paste. The low contrast observed in the micrographs suggests small variations in the surface roughness, with some regions displaying a more compact arrangement of nanoplatelets. The thickness of the GNP coating was measured by using the profilometer (Fig. 2b). The analysis indicated a non-uniform distribution of the coating, with increased thickness at the edges of the sample compared to the central regions. This effect is likely due to the manual deposition process, which leads to material accumulation at the borders. The coating thickness on the silicon rubber is measured to be about 900 nm. AFM measurements (Fig. 2c and d) were conducted to evaluate the nanoscale topography of the GNP-coated surface. The analysis provided insights into the surface roughness (Fig. 2e), revealing an average roughness of a few nanometers over scan areas of a few microns. This relatively low roughness suggests a well-distributed and uniform coating at the nanoscale, which is crucial for optimizing field emission properties and ensuring consistent electron emission across the surface. The morphological and structural characterization confirms that the GNP coating exhibits a layered morphology with controlled thickness variations and a smooth nanoscale roughness, making it a suitable candidate for flexible field emission applications. The adhesion between the GNP coating and the PDMS substrate is primarily ensured by van der Waals forces and mechanical interlocking, favoured by surface roughness and partial embedding of nanoplatelets during the rubbing process. Although no covalent bonding occurs, the interface exhibits robust adhesion, as demonstrated by the coating's mechanical stability under repeated bending.

The crystalline structure of the GNP coating was investigated using X-ray diffraction (XRD) with a Bruker D5000 setup equipped with a Cu Kα excitation source (λ = 0.154 nm) in Bragg–Brentano geometry. This configuration primarily gathers information from lattice planes parallel to the substrate surface. A Ni filter was used to minimize the intensity of the Kβ line in the X-ray spectrum. The XRD spectra were acquired over the 2θ range of 5°–60°. The diffraction pattern is shown in Fig. 3a. The comparative XRD analysis between the silicone

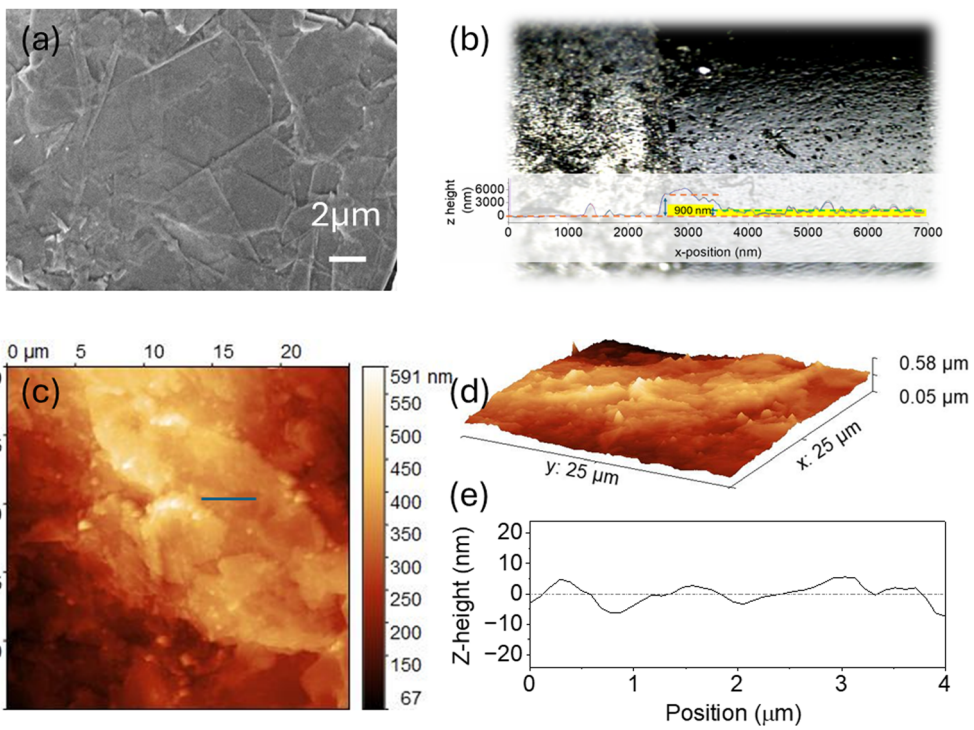

Fig. 2 (a) SEM image of the GNP coating. (b) Optical profilometer image taken at the edge of the sample, showing a step between the uncovered silicone rubber (left) and the GNP coating (right). The inset displays the measured thickness profile. (c) and (d) AFM image of a coating area 25 μm × 25 μm. (e) Line profile extracted from (c) in the position indicated by the blue line.

 This journal is © The Royal Society of Chemistry 2025

Open Access Article. Published on 04 August 2025. Downloaded on 12/21/2025 7:41:02 PM.
This article is licensed under a Creative Commons Attribution 3.0 Unported Licence.

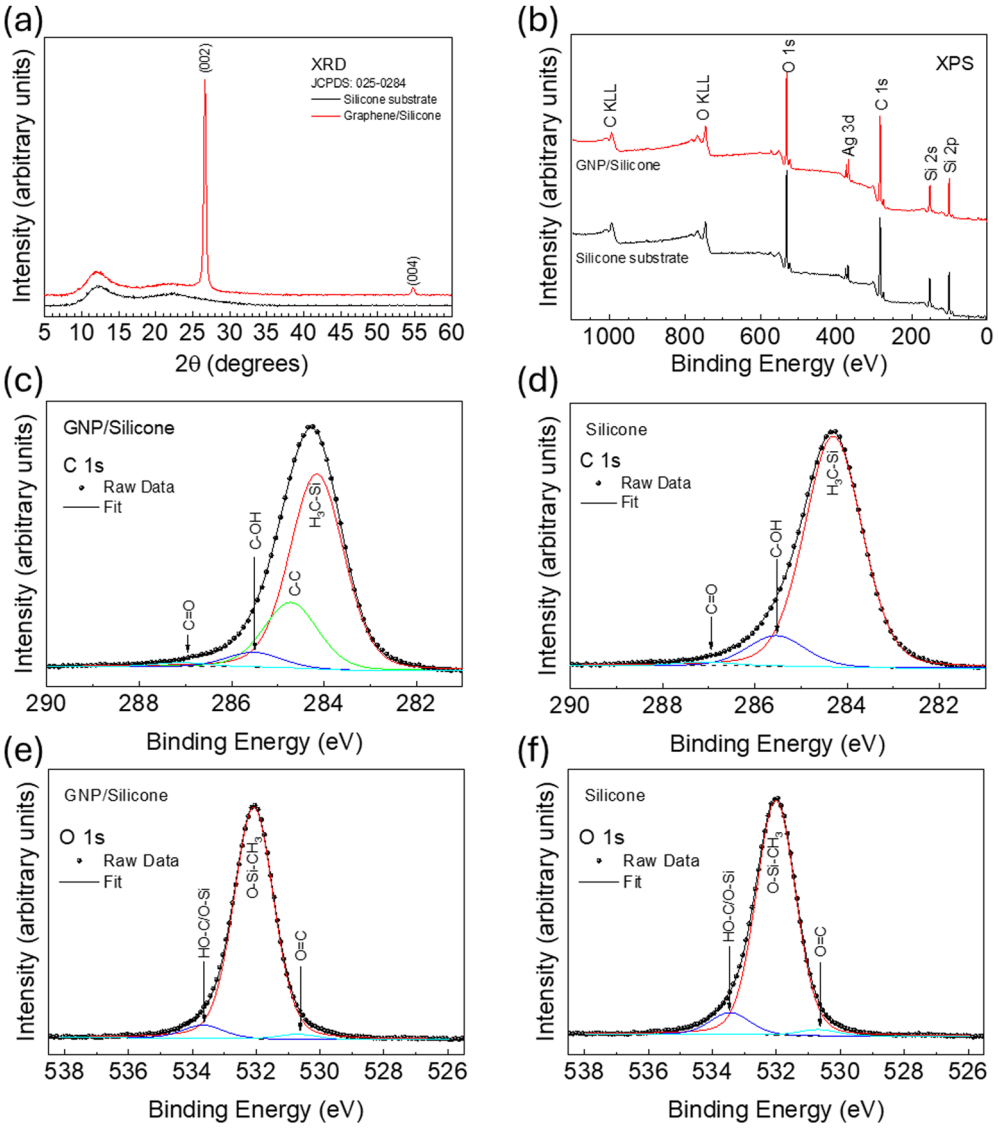

Fig. 3 (a) XRD diffraction patterns of the silicone rubber substrate (black line) and the GNP-coated surface (red line), highlighting the characteristic (002) and (004) peaks of graphitic structures. (b) XPS survey spectra of the GNP/silicone and bare silicone samples. (c) and (d) High-resolution XPS C 1s spectra for the GNP-coated and uncoated surfaces, respectively. (e) and (f) High-resolution XPS O 1s spectra for the GNP-coated and uncoated surfaces, respectively. The presence of prominent C–C and graphitic components in the GNP sample confirms the successful deposition of crystalline nanoplatelets.

rubber substrate and the GNP-coated surface demonstrated that the coating introduces additional peaks corresponding to graphitic planes, while the substrate alone exhibits no significant diffraction features in this region. This confirms the effective deposition of crystalline GNPs on the flexible silicone substrate. The pattern measured on GNP coating revealed a highly crystalline hexagonal structure with no secondary phase or impurity peaks. The most prominent peak at $2\theta = 26.7^\circ$ corresponds to the (002) crystallographic plane of graphitic structures, while a weaker peak at $2\theta = 54.8^\circ$ is attributed to the (004) plane. These observations confirm the presence of well-ordered graphene nanoplatelets within the coating. The broadening of the (002) reflection was used to estimate the mean crystallite size of the GNPs using the Scherrer equation. The analysis determined an average layer size of approximately 19 nm. This thickness value is in excellent agreement with the expected size distribution of graphite nanoplatelets produced *via* thermal exfoliation of graphite bisulfate.[33]

X-ray photoelectron spectroscopy (XPS) was used to determine the elemental composition and chemical state of the elements present in both the GNP coating and the uncovered silicone substrate. The measurements were carried out by means of a PHI 1257 system equipped with a hemispherical analyzer (Physical Electronics Inc.), operating at a pressure below 10^{-9} mbar and utilizing a non-monochromatic Mg Kα source ($h\nu$ = 1253.6 eV). In Fig. 3b, we present the survey spectrum, measured for binding energies (BE) up to 1200 eV, where several peaks corresponding to C, O, Si, and Ag are clearly visible. Silver

Open Access Article. Published on 04 August 2025. Downloaded on 12/21/2025 7:41:02 PM.
This article is licensed under a Creative Commons Attribution 3.0 Unported Licence.

was used to calibrate all XPS spectra. All peaks were deconvoluted using Voigt multi-peaks and a Shirley background. The figure compares the very similar survey spectra obtained from the silicone rubber substrate and the GNP-coated surface. The main difference is observed in the C 1s peak. Specifically, in Fig. 3c and d, we show the C 1s peak measured on the GNP/silicone rubber system and on the uncovered silicone rubber, respectively. In both cases, the peak is located at 284.3 eV and is the result of the convolution of several peaks. Notably, the C–C peak contribution, centered at 284.7 eV, which is clearly visible in the GNP coating, is absent in the silicone rubber spectrum. Additionally, the comparison of the very similar O 1s peaks for the GNP/silicone system (Fig. 3e) and the silicone rubber (Fig. 3f) suggests that there is no significant presence of graphene oxide on the coating's surface.

3.2 Electrical characterization

To investigate the electrical behaviour of the GNP coating, two-probe current–voltage (*I–V*) measurements were performed using a Keithley 4200 source-measurement unit capable of voltage resolution down to few μV and current resolution better than 0.1 pA. For our experiments, silver paste was used to create electrical contacts directly on the GNP coating, avoiding contamination from lithographic processing. We applied the transfer length method (TLM) to extract the contact resistance arising at the Ag/GNP interface. Indeed, TLM is a widely used technique to evaluate the quality of the contact between deposited metal electrodes and the underlying conductive material. In this method, a series of metal pads (see the schematic in Fig. 4a) are placed at different distances, and the total resistance is measured as a function of separation distance between two electrodes. The total resistance is given by $R_{tot} = R_{ch} + 2R_{cont}$ where R_{cont} represents the contact resistance and R_{ch} is the resistance of the conductive coating between adjacent contacts. By extrapolating the linear fit of R_{tot} *versus* the separation distance, the intercept at zero distance provides an estimation of $2R_{cont}$. The TLM structures were tested in a probe station by applying a voltage sweep from −6 V to +6 V while measuring the current. The resulting *I–V* curves were found to be ohmic, indicating a well-formed electrical contact between the GNP coating and the electrodes, for a spacing varying from 4 mm to 25 mm (Fig. 4a). From the TLM measurements it was possible to extract the contact resistance $R_{cont} \approx 95$ kΩ (Fig. 4b). The electrical behaviour was measured across several areas of the sample, confirming the stability and reproducibility of the conductive properties. Long-term stability tests were also conducted by repeating experiments under ambient conditions after one week as well as after one month, after which the

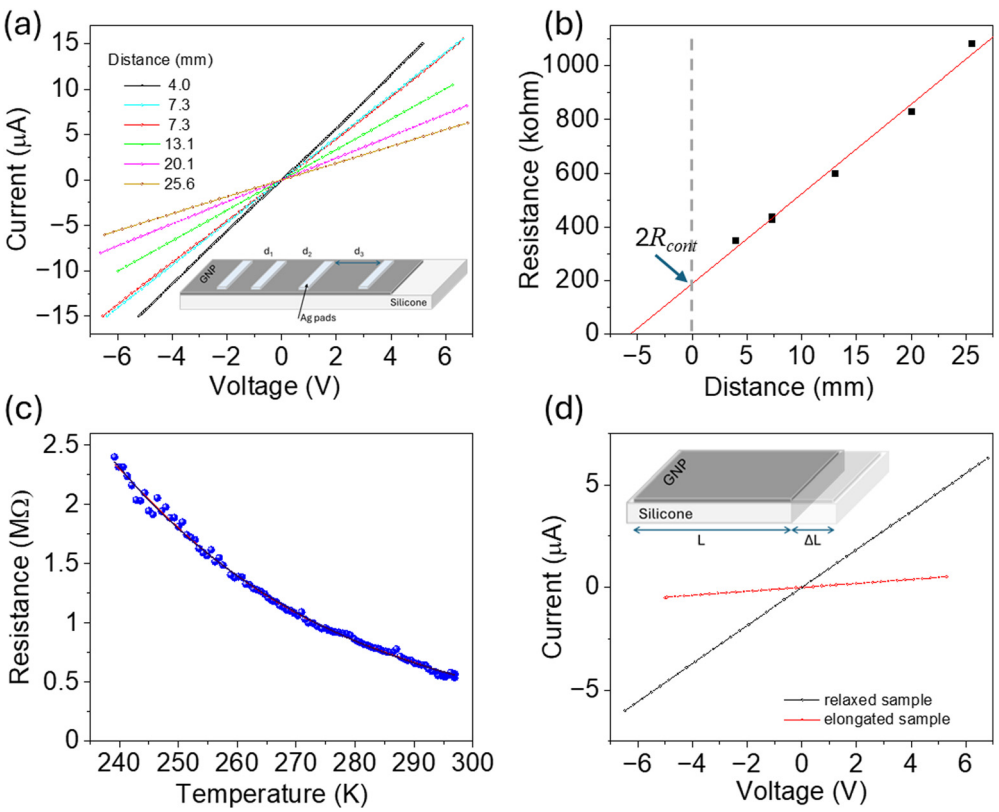

Fig. 4 Electrical characterization of the GNP coating. (a) *I–V* curves measured during the TLM characterization for different contact separations. In the inset: schematic of the sample realized for the TLM measurements. (b) Resistance *versus* distance as measured in the TLM experiment. Red solid line is the linear fit of the experimental data. Intercept gives the value of the contact resistance. (c) Resistance *versus* temperature for the GNP coating measured in the range 240–300 K. Solid line is the numerical fitting to the thermally activated bandgap model. (d) Effect of strain on the GNP conductance. *I–V* characteristics compare the relaxed and the elongated configuration, with $\Delta L = 2\%$.

 This journal is © The Royal Society of Chemistry 2025

Open Access Article. Published on 04 August 2025. Downloaded on 12/21/2025 7:41:02 PM.
This article is licensed under a Creative Commons Attribution 3.0 Unported Licence.

measurements remained unchanged, demonstrating excellent environmental robustness.

The temperature dependence of the resistance $R(T)$ was measured in four probe configuration in the temperature range 240–300 K (it is reported in Fig. 4c). The measurements revealed a negative temperature coefficient of resistance ($dR/dT < 0$), consistent with non-metallic conduction mechanisms. This behavior is commonly observed in carbon-based materials and is generally attributed to mechanisms such as variable range hopping (VRH)[34] or fluctuation-induced tunneling (FIT).[35] The VRH model, often described by Mott's formalism, considers hopping between localized states in disordered systems,[36] while the FIT model describes thermally assisted tunneling across insulating barriers, often relevant for carbon-based systems with conductive regions separated by small gaps. However, the thermally activated barrier model appears as the most suitable for reproducing the experimental data in this case, as confirmed by the numerical fitting shown in Fig. 4c. This model assumes that charge carriers require thermal activation to overcome an energy barrier, leading to a resistance that follows an Arrhenius-type relationship: $\sigma(T) = 1/R(T) = \sigma_0 \exp(-E_g/2k_BT)$, where E_g is the activation energy, k_B is the Boltzmann constant, and T is the temperature. The fit to our experimental data yields an activation energy of 0.31 eV, in line with values (typically ranging between 0.1 eV and 0.4 eV) reported for carbon-based materials with semiconducting-like behaviour, including graphene oxide.[37,38] This agreement confirms a thermally activated transport mechanism in the GNP-coated system. Although models such as VRH are often used to describe conduction in disordered carbon nanostructures like GNPs,[39,40] the relatively high activation energy observed here may instead originate from energy barriers at interflake junctions or charge trapping effects at interfaces, as also supported by studies on similar graphene-based systems.[41–43]

Considering that the GNP coating is deposited on an elastic substrate, we investigated the effect of silicone rubber tensile stress on the conduction of the coating. For this reason, we applied a mechanical force to produce a 2% elongation of the sample under investigation. In Fig. 4d we compare the I–V curves measured for the relaxed sample and the ones for the elongated configuration. It is evident that the effect of elongation is a significant reduction of the conductivity, with the sample resistance that increases of one order of magnitude, from 1.08 MΩ to 10.3 MΩ. This behaviour can be attributed to the mechanical deformation of the GNP network, which affects the connectivity of the conductive pathways. The tensile stress modifies the alignment of the nanoplatelets and increases the spacing between them, reducing the overlap of electronic wavefunctions and affecting charge transport. Moreover, the mechanical deformation could influence the interfacial properties of the GNPs, effectively increasing the energy barrier for charge carrier transport. This is consistent with the thermally

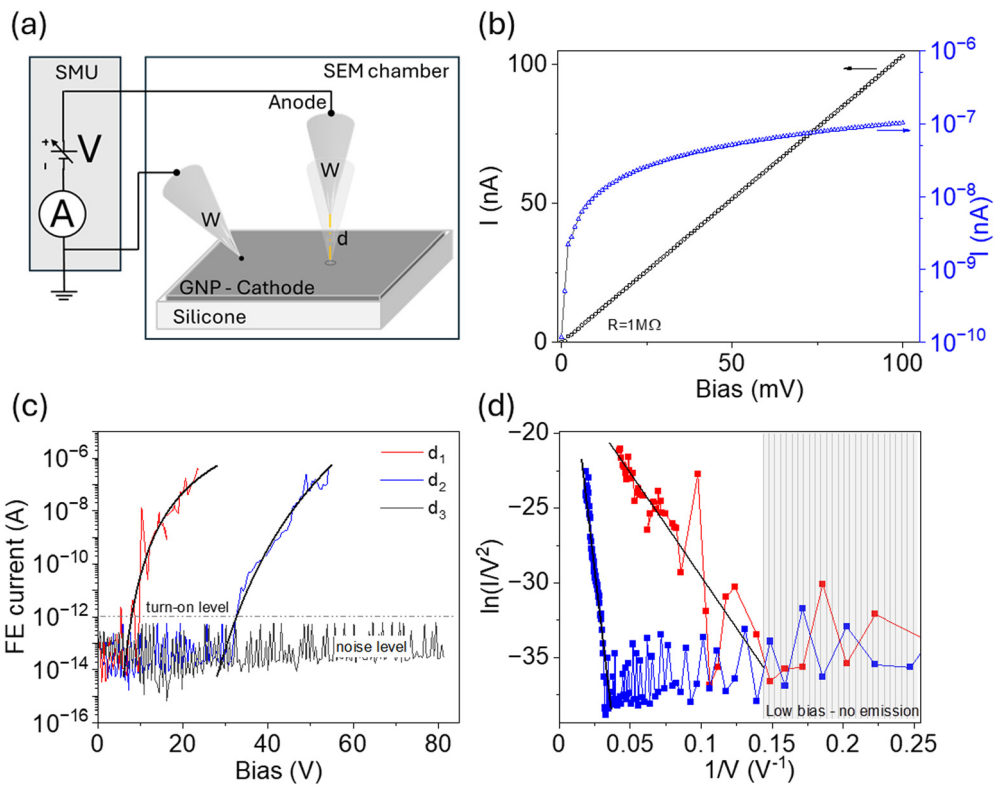

Fig. 5 (a) Schematic of the field emission setup realized inside a SEM chamber. (b) I–V curve measured when both tips are approached on the sample surface, reported in both linear and semilog scale. (c) I–V curves measured in the FE configuration with the tip-anode at three different distances from the emitting surface: d_1 = 100 nm, d_2 = 350 nm, d_3 = 2 μm. Black solid lines represent the numerical fitting to the Fowler–Nordheim model. (d) FN plots for the I–V curves reported in (c). Solid lines are linear fittings of the experimental data.

Open Access Article. Published on 04 August 2025. Downloaded on 12/21/2025 7:41:02 PM.
This article is licensed under a Creative Commons Attribution 3.0 Unported Licence.

activated transport mechanism observed in the temperature dependent measurements, where the conduction is dominated by charge carriers overcoming an activation energy. Similar strain-dependent behaviours have been reported in other graphene-based systems, where mechanical stress reduces the percolative connectivity and increases the effective resistance of the material.[44,45]

3.3 Field emission characterization

Field emission measurements were performed using a scanning electron microscope working at room temperature and a pressure of 10^{-6} mbar, equipped with two piezo-driven probes that can be operated as nano-manipulated electrodes. The vacuum level during the FE measurements is an important parameter, since the presence of adsorbates on the emitter surface, such as O_2, H_2O, *etc.*, significantly affects the emitted current value and stability. A Keithley 4200-SCS source-measurement unit is connected to the metallic probes (tungsten tips) by means of high vacuum feedthroughs, allowing application of voltages up to 200 V, while measuring the current. A schematic of the setup for FE characterization is reported in Fig. 5a, where a tip-shaped anode can be positioned at a controlled distance d from the GNP-coated surface. The anode is a tungsten wire electrochemically etched to obtain an apex with curvature radius of about 100 nm.

By contacting both tips on the GNP surface, we can measure the resistance of the film between the probes. Fig. 5b shows the *I–V* curve measured in this configuration (experimental data are reported in both linear and log scale); this measurement provides an approximate estimation of the series resistance in the FE circuit when one probe (the anode) is retracted for field emission characterization. The tip anode can be positioned in different locations, with step resolution of about 5 nm, and the cathode–anode separation distance, *i.e.* the distance between the metallic tip and the GNP surface, can be directly measured by SEM imaging.

The main advantage of the tip-shaped anode with respect to the standard parallel-plate setup is that it gives access to a local characterization of the field emission properties. Indeed, while the parallel-plate configuration probes emitting areas of several mm^2, the tip anode allows collection of electrons from regions (emitting areas) smaller than 1 μm^2.[46] Indeed, it has been demonstrated that in the tip anode configuration with a cathode–anode separation distance of 200 nm, the effective emitting area is about 0.12 μm^2, and it increases by increasing the separation.

It is important to note that FE curves often exhibit large instabilities (fluctuations and drops) due to the presence and desorption of adsorbates on the emitting surface, which act as nanoprotrusions with a higher field enhancement factor and can evaporate due to Joule heating caused by high FE currents.[47–49] To stabilize the emission, it is possible to perform electrical conditioning by repeating several voltage sweeps before taking measurements.[50,51] The Joule heating, induced by high current densities, can facilitate the gradual desorption of adsorbates from the GNP surface and edge, with nearly complete removal. This process leads to a significant reduction in the noise of the field emission characteristics. In particular, the field emission becomes more stable and reproducible, suggesting that electrical conditioning is an effective method to improve emitter performance by restoring intrinsic emission behaviour. Consequently, we typically perform preliminary electrical conditioning to favour stable performance of the emitters. Current–voltage characteristics have been measured by applying a voltage sweep in the range 0–120 V and measuring the current flowing in the circuit.

In Fig. 5c we show an example of three *I–V* curves measured for different cathode–anode separation distances. When the distance is large, the emission cannot start, and the measured curve (for $d_3 \approx 2$ μm) is simply the floor noise (current level $\sim 10^{-14}$–10^{-13} A) of the setup. We repeat the measurements after reducing the separation distance down to $d_2 = 350$ nm and $d_1 = 100$ nm. In these curves, the emission current remains negligible up to a turn-on voltage (V_{ON}), defined as the applied voltage required to reach a current threshold of 1 pA. A V_{ON} of approximately 8.2 V is measured at a separation distance d_1. As the voltage increases beyond V_{ON}, the current exhibits a rapid exponential increase, consistent with quantum mechanical tunneling of electrons through the potential barrier at the emitter surface. For $d_2 = 350$ nm a turn-on voltage of about 32.6 V is required to initiate the current emission. This observation confirms the expected trend of an increasing turn-on voltage for increasing cathode–anode separation. The emission current increases rapidly by six orders of magnitude from the floor noise level over a bias range of approximately 30 V, starting from V_{ON}. We highlight that we configured the measurement setup to limit the FE current below 1 μA, to prevent setup failure. Indeed, considering an effective emitting area in the order of 0.1 μm^2, we find that a current of 1 μA corresponds to a current density in the order of 10^3 A cm^{-2}.

The experimental current–voltage characteristics were analyzed using the Fowler–Nordheim (FN) model,[5] which describes field emission as a quantum tunneling process under high electric fields. The emitted current is given by the equation:

$$I_{FE} = S{\cdot}a{\cdot}{E_{local}}^{2}\varphi^{-1}{\cdot}\exp(-b{\cdot}{E_{local}}^{-1}\varphi^{3/2})$$

where I_{FE} is the emission current, E_{local} is the local electric field at the emitter surface, φ is the work function of the emitter, S is the effective emitting area, and $a \equiv \frac{e^3}{8\pi h} \approx 1.541 \times 10^{-6}$ A eV V^{-2} and $b \equiv \frac{\left(\frac{8\pi}{3}\right)(2m_e)^{\frac{1}{2}}}{eh} \approx 6.831$ $eV^{-3/2}$ V nm^{-1} are constants. E_{local} takes into account the field enhancement due to the surface morphology and it can be expressed as $E_{local} = \beta{\cdot}E$ where E is the electric field expected in case of a perfect planar metallic emitter surface, and β is the field enhancement factor. In terms of the externally applied bias V, the local field can be expressed as $E_{local} = \beta{\cdot}V/d$.

The experimental data reported in Fig. 5c are compared to simulations according to the FN model evidencing good agreement. Moreover, according to the model, the FN plot ($\ln(I/V^2)$ *vs.* $1/V$) is expected to be linear with slope $m = -(bd\varphi^{3/2})/\beta$ and it can be used to further confirm the FE nature of the measured

 This journal is © The Royal Society of Chemistry 2025

Open Access Article. Published on 04 August 2025. Downloaded on 12/21/2025 7:41:02 PM.
This article is licensed under a Creative Commons Attribution 3.0 Unported Licence.

current. In Fig. 5d, we report the FN plots corresponding to the experimental data measured for d_1 and d_2: the data exhibit a clear linear behaviour, confirming that the measured current originated from a field emission process. Consequently, by performing a linear fit of the FN plot, we can extract the field enhancement factor $\beta = -bd\varphi^{1.5}/m$.

In previous studies, it has been noted that the use of a tip-shaped anode requires the introduction of a correction factor ($k_{tip} \approx 1.6$) to accurately estimate parameters such as the field enhancement factor and the turn-on voltage/field.[52] This correction factor accounts for the geometric influence of the anode tip on the local electric field distribution, which differs from the idealized parallel-plate configuration often assumed in the FN theory. Specifically, the field enhancement factor is corrected as $\beta_{corr} = k_{tip}\beta$, where β_{corr} is the adjusted field enhancement factor and β is the value extracted directly from the FN plot. Similarly, the turn-on field (E_{on}) is adjusted using $E_{on,corr} = E_{on}/k_{tip}$, where $E_{on,corr}$ is the corrected turn-on field value. While the absolute values of these parameters are influenced by the correction factor, it is important to note that the use of k_{tip} does not affect the overall trends observed in the experimental data. The dependence of β and E_{on} on the cathode–anode separation, as well as their variations due to material morphology and local surface conditions, remains consistent before and after applying the correction factor. This ensures that comparative analyses and trend evaluations remain valid, even if absolute parameter values are refined through geometric corrections. We also notice that, in contrast, V_{ON} is not affected by the geometrical correction.

Benefiting from the nanomanipulated tip anode we performed FE measurements by varying the cathode anode separation distance in the range 100 nm $< d <$ 900 nm. The experimental data are summarized in Fig. 6a, showing that the turn-on voltage as a function of the cathode–anode separation distance has a linear dependence. The monotonic trend is expected since field emission is a distance-dependent phenomenon, where a larger separation requires a higher voltage to achieve the necessary local electric field for electron emission. Considering that the separation d is directly measured, and that we can estimate the slope m of the FN plots, we can obtain the field enhancement factor as a function of d, as reported in Fig. 6b. The experimental evidence is that the β factor decreases for increasing d. This behaviour agrees with previous findings reported in the literature for other carbon based nanostructures. For instance, Bonard *et al.*[53] experimentally confirmed this behaviour for individual multi-walled carbon nanotubes, showing that β can reach values as high as $\sim$460 at minimal distances and progressively decreases as the gap increases. Similarly, Smith *et al.*[54] demonstrated that for CNT emitters; Wang *et al.*[55] conducted a systematic field-emission study on

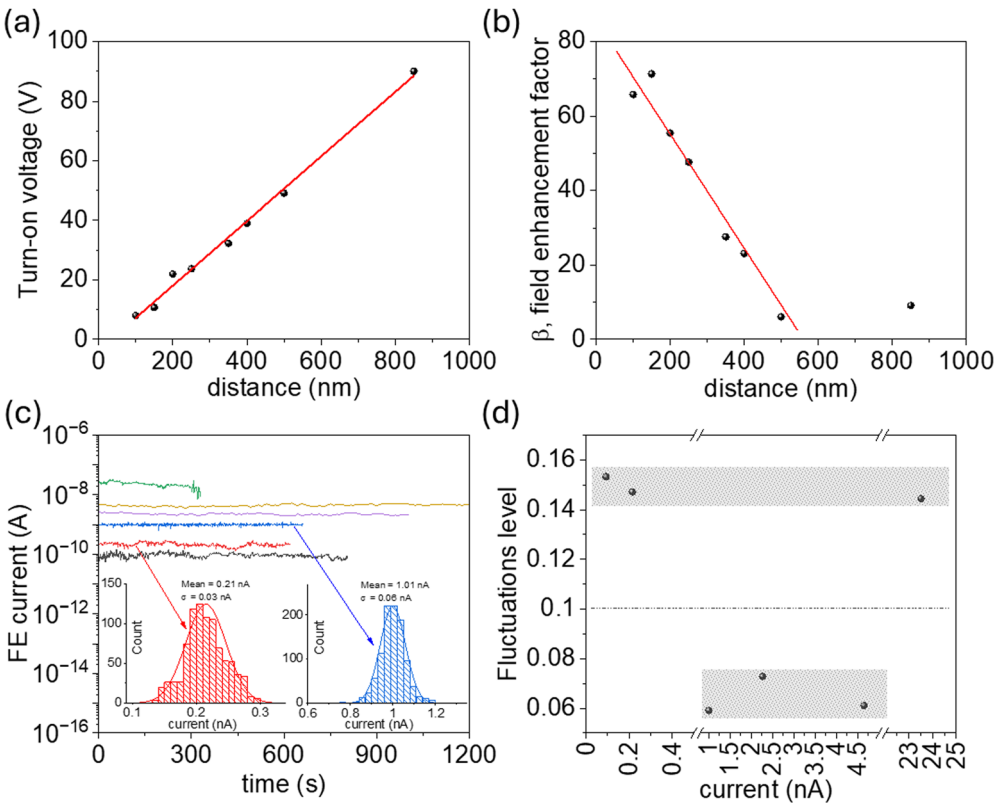

Fig. 6 (a) Turn-on voltage (V_{ON}) as a function of cathode–anode separation distance, showing a monotonic increase with increasing gap. (b) Field enhancement factor, β, extracted from Fowler–Nordheim analysis, decreasing with distance. (c) Temporal stability of the field emission current measured at different current levels; insets show current distributions with average values. (d) Fluctuation levels as a function of emission current, highlighting optimal stability in the 1–5 nA range.

Open Access Article. Published on 04 August 2025. Downloaded on 12/21/2025 7:41:02 PM.
This article is licensed under a Creative Commons Attribution 3.0 Unported Licence.

two-dimensional carbon materials, revealing that β increases with decreasing anode–cathode distance, with experimental data aligning well with their analytical model. Similarly, Passacantando *et al.*[56] investigated field emission from individual multi-walled carbon nanotubes and found that at a cathode–anode distance of approximately 1 μm, the field enhancement factor was around 100, indicating a decrease in β with increasing separation. More recently, a field emission study on graphene nanosheets[16] confirmed that at very small separations ($\sim$400–700 nm), the field enhancement factor is maximized, reaching values of $\sim$32, while increasing the anode distance results in a progressive decline of β. These results support our experimental findings, reinforcing that the field enhancement factor is intrinsically linked to the electrode configuration and decreases as the anode–cathode separation increases.

To evaluate the performance of the GNP emitters, we measured the stability of the FE current over time at different current intensities, as shown in Fig. 6c. The experimental data provide insight into both the stability of the emission and magnitude of the fluctuations. Stability is a critical parameter for FE applications, particularly in vacuum electronic devices, where a steady electron emission is desirable. Fluctuations in the emission current can arise from various factors, including adsorbate dynamics on the emitter surface, structural modifications of the emitting regions, and charge trapping effects.[57–59] The statistical analysis of the emission current, performed across all measured curves, reveals a well-defined distribution, indicating consistent emission properties. However, we identify an optimal operating regime in the current range of 1–5 nA, where fluctuations are minimized (see Fig. 6d). At lower currents, fluctuations increase due to statistical emission noise associated with low electron flux, while at higher currents, instabilities become more pronounced due to local heating effects and potential surface degradation of the emitting sites. These effects have been previously observed in carbon-based emitters, where excessive current densities can induce morphological changes in the emitter, leading to increased fluctuations and long-term degradation.[53,60] Similarly, graphene-based emitters have demonstrated optimal stability in a limited current window, beyond which degradation and emission noise become significant.[16] The field emission performance of GNP coatings is influenced by several key factors: (i) the aspect ratio and sharpness of the nanoplatelet edges, which determine the local electric field enhancement; (ii) the electrical connectivity between flakes, affecting charge transport; (iii) the presence of adsorbates, which may modify emission behaviour or cause instability; and (iv) the geometry of the electrode configuration, particularly the anode–cathode distance. All these aspects contribute to shaping the turn-on voltage and emission stability. Throughout our bending and curvature experiments, the GNP coatings exhibited no evidence of delamination or surface wrinkling. The adhesion to the silicone substrate, primarily governed by van der Waals forces and mechanical interlocking during rubbing, proved to be robust under multiple bending cycles. This mechanical integrity is also supported by the reproducibility of the field emission measurements in both flat and curved configurations. Although detailed wrinkle analysis was not the focus of this study, we are aware that surface wrinkling phenomena in flexible systems may become relevant at smaller scales or under extreme deformation, as discussed in recent studies on polymeric and curved substrates.[61,62]

3.4 Flexible FE cathodes

To investigate how mechanical deformation affects electron emission and provides insight into the feasibility of employing these cathodes in bendable and stretchable electronic devices, we studied the field emission properties of the cathode with different curvature radii.

In Fig. 7a and b, SEM images show two different configurations obtained by bending the GNP/silicone rubber system: a large curvature radius configuration with r_L = 4.1 mm and a small curvature radius configuration with r_s = 2.6 mm, respectively. As for the flat sample, the FE characterization was repeated by approaching the tip anode at a controlled distance from the emitting surface, and FE current was measured while sweeping a voltage bias up 100 V. The current–voltage characteristics were measured for both configurations by varying the cathode–anode separation distance in the range 100–900 nm. The measured *I–V* curves are reported in Fig. 7c and d for the r_L and r_s configurations, respectively. We notice that, as expected, by increasing the separation distance, the turn-on voltage increases in both cases. As confirmation of the FE nature of the measured currents, we also show in Fig. 7e and f the correspondent FN plots along with their linear fittings. In both configurations, the nanoplatelets maintain their layered structure, but the surface geometry alters the spatial orientation of their edges.

In the case of the large curvature radius, the bending is gentle and the nanoplatelets tend to follow the surface profile with limited deviation from planarity. For the small curvature radius, the sharper bending induces more pronounced tilting and slight exposure of the platelet edges from the substrate. This increased edge exposure favours the local electric field concentration at these sites, thereby favouring field emission. Such morphological changes are consistent with the expected field enhancement mechanisms in 2D carbon materials, where the edge sharpness and angular orientation with respect to the applied field play a crucial role.

The FE properties in the three different configurations are summarized in Fig. 8. A schematic representation of how increasing curvature induces a morphological reconfiguration of the graphite nanoplatelets is given in Fig. 8a. Specifically, sharper bending promotes the tilting of the nanoplatelets from the substrate, leading to an increased exposure of edge sites. This reorganization modifies the local electric field distribution, slightly influencing the electron emission characteristics. In Fig. 8b, we show that experimental data provide a clear inverse correlation between the turn-on voltage and the normalized field enhancement parameter β/d: higher β/d values correspond to lower V_{ON}, reinforcing the interpretation that sharper bending (which increases β) reduces the energy barrier for emission onset. In Fig. 8c, we compare the turn-on voltage as a function of anode–cathode distance for flat, large curvature radius and small curvature radius configurations. All configurations exhibit very similar linear

 This journal is © The Royal Society of Chemistry 2025

Open Access Article. Published on 04 August 2025. Downloaded on 12/21/2025 7:41:02 PM.
This article is licensed under a Creative Commons Attribution 3.0 Unported Licence.

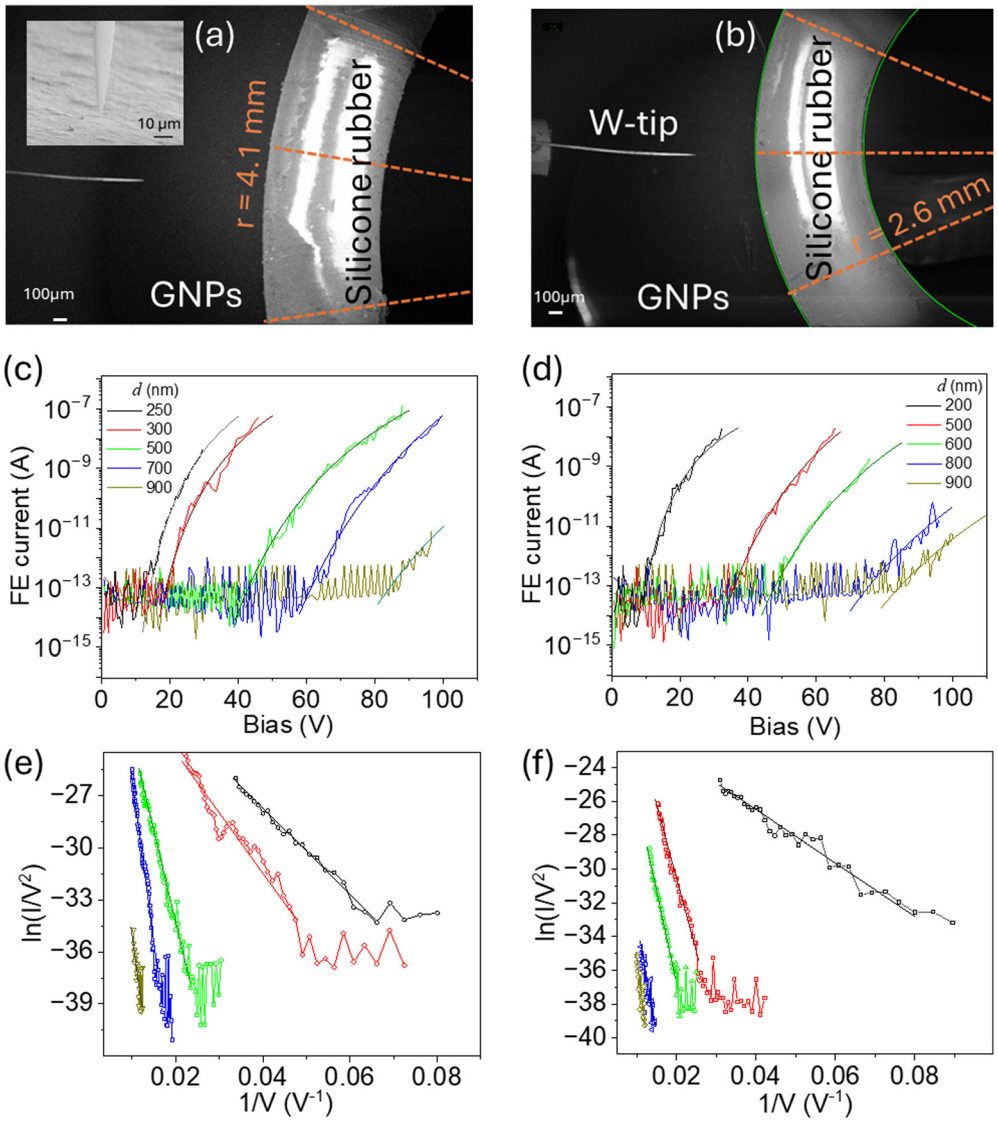

Fig. 7 SEM image of the GNP/silicone rubber system in the bended configuration with curvature radius (a) r_L = 4.1 mm and (b) r_s = 2.6 mm. The inset in (a) shows a magnification of the tungsten tip anode approaching the sample surface. (c) and (d) *I*–*V* curves measured for different values of the anode–cathode separation distance in the range 100–900 nm for r_L and r_s, respectively. Solid lines represent the numerical fitting to the Fowler–Nordheim model. (e) and (f) FN plots corresponding to the *I*–*V* curves reported in (c) and (d), respectively. Solid lines represent the linear fittings of the data.

dependence of V_{ON} on distance. The flat sample consistently shows slightly higher V_{ON} values at the same separation. This could be attributed to the more homogeneous and planar distribution of nanoplatelets in the flat state, which leads to lower local field concentrations compared to the curved cases where nanoplatelet misalignment and edge protrusion enhance the effective field.

In Fig. 8d, we finally report the extracted field enhancement factor β as a function of distance for the three curvature regimes. The small curvature radius configuration exhibits the highest β values across the explored distance range. This enhancement is consistent with previous observations in carbon-based emitters, including carbon nanotubes and graphene sheets, where structural protrusions and angular edge alignment significantly increase local electric fields. It is worth noting that the variation in field emission performance induced by different curvature radii is fully reversible and reproducible. No degradation of the emission properties was observed after repeated bending cycles, indicating that the modulation introduced by curvature does not compromise the stability of the device. Instead, it enables a reliable and controllable tuning mechanism based on the mechanical deformation of the substrate.

4. Conclusions

We have demonstrated a scalable and effective strategy for the realization of flexible cold cathodes based on graphite nanoplatelet coatings on silicone rubber substrates. Through comprehensive morphological, structural, electrical, and field emission characterizations, we establish the strong potential

Open Access Article. Published on 04 August 2025. Downloaded on 12/21/2025 7:41:02 PM.
This article is licensed under a Creative Commons Attribution 3.0 Unported Licence.

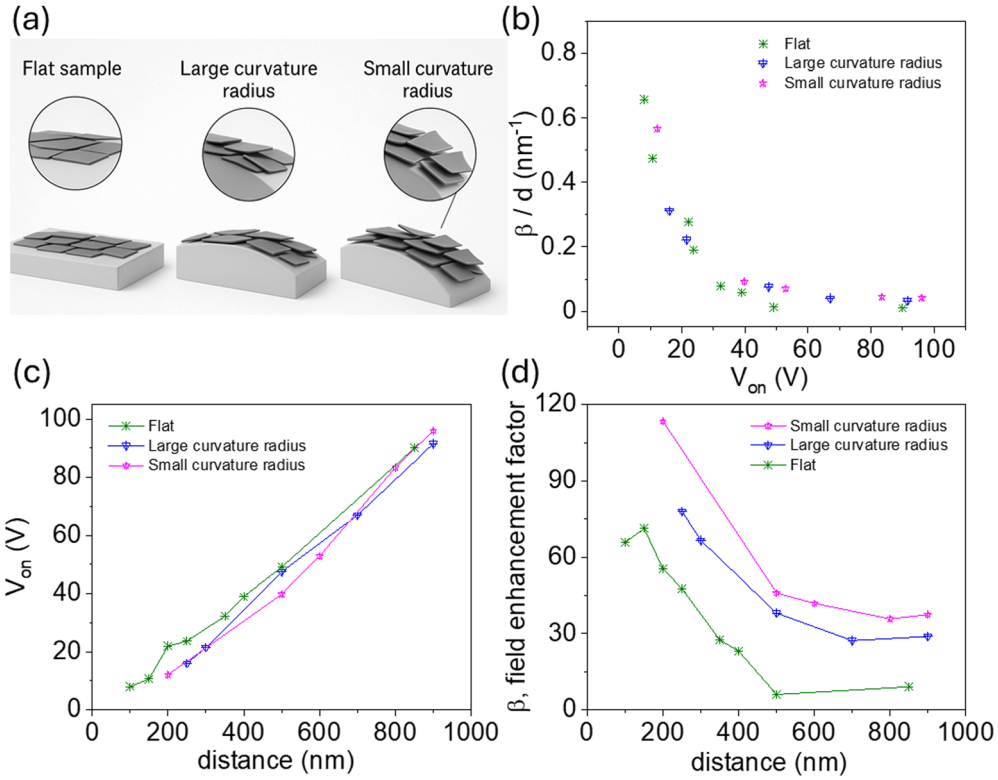

Fig. 8 (a) Schematic representation of the morphological evolution of GNP alignment under increasing substrate curvature. With sharper bending, nanoplatelets exhibit enhanced edge tilting and partial delamination, which amplify local electric fields. (b) Experimental correlation between normalized field enhancement factor (β/d) and turn-on voltage across different curvature regimes. (c) Turn-on voltage as a function of anode–cathode separation distance for flat, large-radius, and small-radius configurations, exhibiting linear trends. (d) Field enhancement factor β *versus* cathode–anode distance, showing a systematic increase in β with decreasing curvature radius.

of this platform for vacuum electronic applications. The GNP films exhibit robust electron emission with low turn-on voltages, high field enhancement factors, and remarkable mechanical adaptability. Our study shows that substrate curvature modulates the emission behaviour by affecting edge exposure and the local electric field distribution. The results pave the way for the integration of GNP-based cathodes in next-generation vacuum electronic devices. Future efforts may focus on engineering curvature-responsive architectures and exploring combinations with other low-dimensional materials to further expand the functionality of flexible electron sources.

Author contributions

F. Giubileo: conceptualization, methodology, investigation, formal analysis, data curation, visualization, writing – original draft, writing – review & editing, supervision, project administration. G. Carotenuto: methodology, resources, writing – review & editing. A. Longo: methodology, resources, writing – review & editing. M. Palomba: methodology, resources, writing – review & editing. E. Faella: investigation, formal analysis, data curation. M. Lettieri: investigation, visualization, data curation. L. Viscardi: investigation, visualization, data curation. K. Intonti: investigation, visualization, data curation. A. Kumar: investigation, visualization, data curation. A. Pelella: visualization, formal analysis, data curation. M. Passacantando: resources, methodology, investigation, data curation. A. Di Bartolomeo: resources, conceptualization, methodology, supervision, writing – review & editing.

Conflicts of interest

There are no conflicts to declare.

Data availability

The data supporting this article have been included as part of the SI. The SI includes figures showing the preparation of graphite nanoplatelets, their thickness and structural characterization (AFM, XRD, XPS), transport measurements (TLM, resistance–temperature, *I–V* behavior), and detailed field emission studies covering turn-on voltage, field enhancement factors, distance dependence, time stability, and fluctuations. See DOI: **https://doi.org/10.1039/d5tc02257f**

Acknowledgements

We acknowledge financial support under the National Recovery and Resilience Plan (NRRP), Mission 4, Component 2, Investment 1.1, Call for tender No. 1409 published on 14.9.2022 by the Italian Ministry of University and Research (MUR), funded

 This journal is © The Royal Society of Chemistry 2025

by the European Union – NextGenerationEU – Project Title "Development of two-dimensional environmental gas nanosensors with enhanced selectivity through fluctuation spectroscopy" (2DEGAS) – CUP B53D23028650001 – Grant Assignment Decree No. 1381 adopted on 01.9.2023 by the Italian Ministry of Ministry of University and Research (MUR).

Open Access Article. Published on 04 August 2025. Downloaded on 12/21/2025 7:41:02 PM. This article is licensed under a Creative Commons Attribution 3.0 Unported Licence.

References

1 I. Brodie and P. Schwoebel, eds, *Field Emission in Vacuum Microelectronics*, Springer, US, Boston, MA, 2005.
2 G. N. Fursey, *Appl. Surf. Sci.*, 2003, **215**, 113–134.
3 S. Zhou, K. Chen, M. T. Cole, Z. Li, J. Chen, C. Li and Q. Dai, *Adv. Mater.*, 2019, **31**, 1805845.
4 H. Y. Kim, M. Garg, S. Mandal, L. Seiffert, T. Fennel and E. Goulielmakis, *Nature*, 2023, **613**, 662–666.
5 R. H. Fowler and L. Nordheim, *Proc. R. Soc. A*, 1928, **119**, 173–181.
6 F. Giubileo, A. Di Bartolomeo, L. Iemmo, G. Luongo and F. Urban, *Appl. Sci.*, 2018, **8**, 526.
7 Y. J. Zeng, S. S. Lin, A. Volodin, Y. F. Lu, Z. Z. Ye and C. Van Haesendonck, *Appl. Phys. Lett.*, 2010, **97**, 143102.
8 A. Di Bartolomeo, M. Passacantando, G. Niu, V. Schlykow, G. Lupina, F. Giubileo and T. Schroeder, *Nanotechnology*, 2016, **27**, 485707.
9 D. Xiao, H. Du, L. Sun, X. Suo, Y. Wang, Y. Zhang, S. Zhang, S. Kuang, F. Hu, L. Tu, D. Yu and P. Song, *Nat. Commun.*, 2024, **15**, 764.
10 H. Su, Y. Guo, X. Yang, C. Liu, X. Li, H. Jiang, M. Yu, H. Fan, M. Guo, Z. Zhang and W. Ren, *Adv. Funct. Mater.*, 2024, **34**, 2406038.
11 F. Giubileo, E. Faella, A. Pelella, A. Kumar, D. Capista, M. Passacantando, S. S. Kim and A. Di Bartolomeo, *Adv. Electron. Mater.*, 2022, **8**, 2200237.
12 N. U. Kiran, A. B. Deore, M. A. More, D. J. Late, C. S. Rout, P. Mane, B. Chakraborty, L. Besra and S. Chatterjee, *ACS Appl. Electron. Mater.*, 2022, **4**, 2656–2666.
13 K. Kobashi, T. Tachibana, C. Ichihara and A. Kobayashi, *Diamond Relat. Mater.*, 2009, **18**, 1081–1084.
14 F. Giubileo, E. Faella, A. Kumar, S. De Stefano, L. Viscardi, K. Intonti, O. Durante, A. Pelella, A. Mazzotti, N. Martucciello, E. Beliayev, Y. K. Mishra, M. Passacantando and A. Di Bartolomeo, *Nano Express*, 2024, **5**, 045017.
15 P. K. Bankar, B. R. Thombare, D. S. Gavhane, S. Kulkarni, G. S. Lole, K. D. Daware, M. M. More, S. I. Patil and P. R. Dusane, *J. Mater. Sci.: Mater. Electron.*, 2024, **35**, 1214.
16 F. Giubileo, D. Capista, E. Faella, A. Pelella, W. Y. Kim, P. Benassi, M. Passacantando and A. Di Bartolomeo, *Adv. Electron. Mater.*, 2023, **9**, 2200690.
17 S. Iijima, *Nature*, 1991, **354**, 56–58.
18 J.-M. Bonard, H. Kind, T. Stöckli and L.-O. Nilsson, *Solid-State Electron.*, 2001, **45**, 893–914.
19 L. Iemmo, A. Di Bartolomeo, F. Giubileo, G. Luongo, M. Passacantando, G. Niu, F. Hatami, O. Skibitzki and T. Schroeder, *Nanotechnology*, 2017, **28**, 495705.
20 M. Palomba, G. Carotenuto, A. Longo, A. Sorrentino, A. Di Bartolomeo, L. Iemmo, F. Urban, F. Giubileo, G. Barucca, M. Rovere, A. Tagliaferro, G. Ambrosone and U. Coscia, *Materials*, 2019, **12**, 3638.
21 Y. Song, D. Hoon Shin, Y.-H. Song, Y. Saito and C. Jin Lee, *Appl. Phys. Lett.*, 2013, **103**, 073112.
22 M. Ojrzyńska, J. Jamroz, M. Maciałowicz, K. Wilczyński, A. Daniszewska, J. Antonowicz and M. Zdrojek, *Mater. Today Commun.*, 2025, **42**, 111543.
23 P. Cataldi, A. Athanassiou and I. S. Bayer, *Appl. Sci.*, 2018, **8**(9), 1438.
24 K. R. Paton, E. Varrla, C. Backes, R. J. Smith, U. Khan, A. O'Neill, C. Boland, M. Lotya, O. M. Istrate, P. King, T. Higgins, S. Barwich, P. May, P. Puczkarski, I. Ahmed, M. Moebius, H. Pettersson, E. Long, J. Coelho, S. E. O'Brien, E. K. McGuire, B. M. Sanchez, G. S. Duesberg, N. McEvoy, T. J. Pennycook, C. Downing, A. Crossley, V. Nicolosi and J. N. Coleman, *Nat. Mater.*, 2014, **13**, 624–630.
25 C.-H. Chen, S.-W. Yang, M.-C. Chuang, W.-Y. Woon and C.-Y. Su, *Nanoscale*, 2015, **7**, 15362–15373.
26 Y. Hernandez, V. Nicolosi, M. Lotya, F. M. Blighe, Z. Sun, S. De, I. T. McGovern, B. Holland, M. Byrne, Y. K. Gun'Ko, J. J. Boland, P. Niraj, G. Duesberg, S. Krishnamurthy, R. Goodhue, J. Hutchison, V. Scardaci, A. C. Ferrari and J. N. Coleman, *Nat. Nanotechnol.*, 2008, **3**, 563–568.
27 M. Lotya, Y. Hernandez, P. J. King, R. J. Smith, V. Nicolosi, L. S. Karlsson, F. M. Blighe, S. De, Z. Wang, I. T. McGovern, G. S. Duesberg and J. N. Coleman, *J. Am. Chem. Soc.*, 2009, **131**, 3611–3620.
28 S. H. Lee, J. S. Han, H. Go and C. J. Lee, *AIP Adv.*, 2021, **11**, 035307.
29 S. Chen and W. Yang, *J. Mater. Chem. C*, 2017, **5**, 10682–10700.
30 E. Forestier, M. Najafi, S. Dussoni, M. Maggiali, A. Athanassiou and I. S. Bayer, *Prog. Org. Coat.*, 2023, **174**, 107251.
31 G. Carotenuto, A. Longo, L. Nicolais, S. De Nicola, E. Pugliese, M. Ciofini, M. Locatelli, A. Lapucci and R. Meucci, *J. Phys. Chem. C*, 2015, **119**, 15942–15947.
32 U. Coscia, M. Palomba, G. Ambrosone, G. Barucca, M. Cabibbo, P. Mengucci, R. De Asmundis and G. Carotenuto, *Nanotechnology*, 2017, **28**, 194001.
33 L. M. Viculis, J. J. Mack, O. M. Mayer, H. T. Hahn and R. B. Kaner, *J. Mater. Chem.*, 2005, **15**, 974–978.
34 K. B. Efetov, *Adv. Phys.*, 1983, **32**, 53–127.
35 P. Sheng, *Phys. Rev. B: Condens. Matter Mater. Phys.*, 1980, **21**, 2180–2195.
36 D. J. Sánchez-Trujillo, L. V. Osorio-Maldonado and J. J. Prías-Barragán, *Sci. Rep.*, 2023, **13**, 4810.
37 J. Lee, J. B. Ferguson, A. M. Hubbard, Y. Ren, D. Nepal, T. C. Back, N. R. Glavin and A. K. Roy, *Mater. Today Commun.*, 2024, **39**, 108859.
38 S. Gong, Z. H. Zhu and Z. Li, *Phys. Chem. Chem. Phys.*, 2017, **19**, 5113–5120.
39 G. Goracci and J. S. Dolado, *Materials*, 2020, **13**, 275.
40 D. Joung and S. I. Khondaker, *Phys. Rev. B: Condens. Matter Mater. Phys.*, 2012, **86**, 235423.

Open Access Article. Published on 04 August 2025. Downloaded on 12/21/2025 7:41:02 PM.
This article is licensed under a Creative Commons Attribution 3.0 Unported Licence.

41 C. Lampadaris, I. Sakellis and A. N. Papathanassiou, *Appl. Phys. Lett.*, 2017, **110**, 222901.
42 R. Debbarma, S. Behura, P. Nguyen, T. S. Sreeprasad and V. Berry, *ACS Appl. Mater. Interfaces*, 2016, **8**, 8721–8727.
43 R. Islam, A. N. Papathanassiou, R. Chan Yu King, J.-F. Brun and F. Roussel, *Appl. Phys. Lett.*, 2015, **107**, 053102.
44 U. Coscia, A. Longo, M. Palomba, A. Sorrentino, G. Barucca, A. Di Bartolomeo, F. Urban, G. Ambrosone and G. Carotenuto, *Coatings*, 2021, **11**, 332.
45 Y. Liu, D. Zhang, K. Wang, Y. Liu and Y. Shang, *Composites, Part A*, 2016, **80**, 95–103.
46 F. Giubileo, E. Faella, D. Capista, M. Passacantando, O. Durante, A. Kumar, A. Pelella, K. Intonti, L. Viscardi, S. De Stefano, N. Martucciello, M. F. Craciun, S. Russo and A. Di Bartolomeo, *Nanoscale*, 2024, **16**, 16718–16728.
47 K. S. Yeong and J. T. L. Thong, *Appl. Surf. Sci.*, 2004, **233**, 20–23.
48 E. Rahman and A. Nojeh, *Nanotechnology*, 2019, **30**, 175202.
49 L. Jiang, P. Liu, L. Zhang, C. Liu, L. Zhang and S. Fan, *RSC Adv.*, 2018, **8**, 31830–31834.
50 R. Riccitelli, A. Di Carlo, A. Fiori, S. Orlanducci, M. L. Terranova, A. Santoni, R. Fantoni, A. Rufoloni and F. J. Villacorta, *J. Appl. Phys.*, 2007, **102**, 054906.
51 F. Giubileo, A. D. Bartolomeo, A. Scarfato, L. Iemmo, F. Bobba, M. Passacantando, S. Santucci and A. M. Cucolo, *Carbon*, 2009, **47**, 1074–1080.
52 A. Di Bartolomeo, A. Scarfato, F. Giubileo, F. Bobba, M. Biasiucci, A. M. Cucolo, S. Santucci and M. Passacantando, *Carbon*, 2007, **45**, 2957–2971.
53 J.-M. Bonard, K. A. Dean, B. F. Coll and C. Klinke, *Phys. Rev. Lett.*, 2002, **89**, 197602.
54 R. C. Smith and S. R. P. Silva, *J. Appl. Phys.*, 2009, **106**, 014314.
55 Y. Wang, Y. Yang, Z. Zhao, C. Zhang and Y. Wu, *Appl. Phys. Lett.*, 2013, **103**, 033115.
56 M. Passacantando, F. Bussolotti, S. Santucci, A. Di Bartolomeo, F. Giubileo, L. Iemmo and A. M. Cucolo, *Nanotechnology*, 2008, **19**, 395701.
57 S. Kita, Y. Sakai, T. Endo, W. Sugimoto and H. Goto, *J. Vac. Sci. Technol., B: Nanotechnol. Microelectron.: Mater., Process., Meas., Phenom.*, 2012, **30**, 031801.
58 N. Shimoi and K. Tohji, *Appl. Sci.*, 2017, **7**, 1322.
59 F. Giubileo, A. D. Bartolomeo, A. Scarfato, L. Iemmo, F. Bobba, M. Passacantando, S. Santucci and A. M. Cucolo, *Carbon*, 2009, **47**, 1074–1080.
60 J.-M. Bonard, C. Klinke, K. A. Dean and B. F. Coll, *Phys. Rev. B: Condens. Matter Mater. Phys.*, 2003, **67**, 115406.
61 X. Gong, T. Hu, Y. Zhang, Y. Zeng, Y. Zhang, Z. Jiang, Y. Tan, Y. Zou, J. Wang, J. Dai and Z. Chu, *Nano-Micro Lett.*, 2024, **16**, 243.
62 S. Zhong, W. Liang, H. Zhong, Y. Zou, S. Lu, R. Chen, Z. Yuan and X. Chen, *Mater. Today Chem.*, 2025, **47**, 102892.

 This journal is © The Royal Society of Chemistry 2025